remote sensing

MDPI

Article

Utilizing Ground-Penetrating Radar for Water Leak Detection and Pipe Material Characterization in Environmental Studies: A Case Study

Mohamed Gamal [1,2,3,4], Qingyun Di [1,2,4,*], Jinhai Zhang [1,2], Changmin Fu [1,2,4], Shereen Ebrahim [5] and Amr Abd El-Raouf [6]

1 Engineering Laboratory for Deep Resources Equipment and Technology, Institute of Geology and Geophysics, Chinese Academy of Sciences, Beijing 100029, China; mohamed_gamal@science.suez.edu.eg (M.G.); zjh@mail.iggcas.ac.cn (J.Z.); fcm168@mail.iggcas.ac.cn (C.F.)
2 Innovation Academy for Earth Science, Chinese Academy of Sciences, Beijing 100029, China
3 Department of Geology, Faculty of Science, Suez Canal University, Ismailia 41522, Egypt
4 College of Earth and Planetary Sciences, University of Chinese Academy of Sciences, Beijing 100049, China
5 National Research Institute of Astronomy and Geophysics, Helwan 11421, Egypt; sherinsa@nriag.sci.eg
6 Department of Geology, Faculty of Science, Zagazig University, Zagazig 44519, Egypt; ammohammed@science.zu.edu.eg
* Correspondence: qydi@mail.iggcas.ac.cn

Abstract: Detecting and mapping subsurface utilities in urban areas is crucial for identifying defects or damages in drinking and sewage pipes that can cause leaks. These leaks make it difficult to accurately characterize the pipes due to changes in their reflective properties. This study focused on detecting leaks originating from underground pipes and distinguishing between these various types of pipes. It also aimed to create a visual fingerprint model that displays the reflection characteristics of these pipes during different leak conditions, enabling efficient maintenance and handling procedures on the pipes. To achieve this, a finite-difference time-domain (FDTD) method was used to simulate two types of pipe materials with and without leak areas to construct different scenarios. Additionally, a ground-penetrating radar (GPR) field survey was conducted using a 600 MHz antenna in a part of the El Hammam area on Egypt's northwest coast. The simulated images produced with numerical modeling were compared with the radar profiles obtained using GPR at particular locations. The numerical simulations and radar profiles demonstrated the noticeable influence of water leaks from the different pipes, wherein the reflection of saturated soil waves was interrupted due to the presence of saturated soil. Envelope and migration techniques were employed in a new application to accurately distinguish between different pipe types, specifically focusing on leak areas. The strong correlation between the real radar profile and the specific signal of a water pipe leak in the simulated models suggests that GPR is a reliable non-destructive geophysical method for detecting water pipe leaks and distinguishing between the different pipe materials in various field conditions. The simulated models, which serve as image-matching fingerprints to identify and map water pipe leaks, help us to comprehend reality better.

Keywords: leaks; underground pipes; FDTD; GPR; numerical modeling; trace analysis; envelope; migration

Citation: Gamal, M.; Di, Q.; Zhang, J.; Fu, C.; Ebrahim, S.; El-Raouf, A.A. Utilizing Ground-Penetrating Radar for Water Leak Detection and Pipe Material Characterization in Environmental Studies: A Case Study. *Remote Sens.* **2023**, *15*, 4924. https://doi.org/10.3390/rs15204924

Academic Editors: Pier Matteo Barone, Alastair Ruffell and Carlotta Ferrara

Received: 2 September 2023
Revised: 7 October 2023
Accepted: 9 October 2023
Published: 12 October 2023

1. Introduction

In recent years, water leaks from distribution pipes have become a significant concern in many water distribution systems. As outlined by the authors in [1], these leaks can significantly affect the environment and infrastructure, causing problems including groundwater pollution, freshwater loss, and ground subsidence. The possibility that the water, which was previously safe at the source, becomes contaminated before it reaches the customer

increases if there is a leak in the underground water distribution piping system. To address this issue, it is essential to detect and locate leaks, and repair the pipes responsible for these leaks within water networks. Early detection of anomalies and the precise identification of flaw locations are crucial to overcoming this problem efficiently. The most commonly used methods for detecting leaks in water networks include the acoustic method [2,3], infrared thermography [4], gas trace test, and GPR [5,6]. While these methods can be effective, GPR is beneficial for characterizing ground conditions in urban areas and is considered one of the most effective tools available [7]. This is because GPR can identify contrasts between leaked water and the surrounding ground by analyzing dielectric characteristics and can be used to create radargrams that aid in water network inspection [8]. GPR is a promising method for detecting leaks in both metal and PVC pipes; it can detect anomalous changes—caused by water saturation or by recognizing subsurface voids produced by water that has spilled and corroded the material surrounding the pipe—in the characteristics of the material next to the pipes [9,10]. Regardless of the pipe's material, whether metal or PVC, GPR can detect leaks. Due to this advantage, GPR is a more promising choice than conventional acoustic leak detection techniques, which frequently encounter difficulties when used with PVC pipelines [11]. Consequently, GPR has recently been increasingly used for subsurface geophysical investigations, especially at shallow depths [12]. Although GPR is an easy and fast methodology, interpreting the obtained images can be challenging [13]. For an accurate visualization of buried pipes and water leaks, it is necessary to treat the images adequately by applying different processes and filters [14] that enhance the visualization of the desired characteristics.

GPR is a current surface geophysical survey technique that has advanced significantly in the past 30 years for shallow and highly accurate exploration; it is also safe for use in urban environments to identify buried objects and determine the subsurface structure and properties [15]. It is the most widely used technique for shallow subsurface investigation [16,17], geotechnical investigation [18,19], archaeology [20,21], underground structural exploration on the Moon [22,23] and Mars [24], environmental and engineering studies [7,25,26] for detecting water leaks around artificial buildings, and the detection of subsurface utilities [27–30].

The efficiency of locating buried objects, including pipelines, and identifying leaks in buried pipelines using GPR images can vary depending on the processing methodology applied. Several studies have explored different approaches to processing GPR images for this purpose. For example, a comparison was made between synthetic GPR signatures for leaking and non-leaking pipes using different configurations to simulate the GPR response of leaking buried pipes [31]. An extensive survey was conducted to evaluate the potential of using GPR for leak detection [11]. The GPR approach efficiently detects pipe leaks and provides details on the pipeline's soil characteristics [32]. Low-band filters were used to detect leaks in PVC urban pipelines [33]. The Hough transform technique was employed to identify and locate hyperbolic patterns to recognize the presence of the target [34]. The Hilbert and Fourier transforms were utilized to demonstrate anomalies based on their magnitude, phase, and frequency [35]. A multi-agent approach was developed to examine and detect plastic pipes hidden within water supply systems [13]. Signature images were collected to detect water leaks by utilizing differences in the dielectric contrast and reflection coefficient during different stages of water injection [36]. Laboratory experiments were conducted to evaluate the ability of GPR technology to detect water leaks in metal and PVC pipes [10]. Diffraction imaging, numerical simulation, and both 2D and 3D GPR survey lines were utilized to enhance the imaging and characterization of water leaks [37].

Once leaks have been detected, it is crucial to quickly identify the type of pipe materials and the exact locations and depths of the pipes responsible before excavation to facilitate prompt maintenance and damage repair [38]. Previously, numerous studies have concluded that the GPR technique is effective, particularly in accurately differentiating between metal and non-metal materials. For instance, experiments were carried out in a water environment to assess various types of pipelines by using travel-time calculations [39]. A 200 MHz GPR

system was utilized to evaluate three spectral features to distinguish between concrete, metallic, and plastic materials [40]. The best frequency for detecting various types of pipes was determined based on the characteristics of the soil textures [41]. However, previous studies have not adequately addressed the specific challenge of distinguishing between these pipes within leak areas. While the detection of these pipes within dry areas is relatively straightforward, it becomes challenging within areas affected by leaks. This prompted our study to explore a new application using envelope and migration techniques to address and resolve this problem.

This study aimed to identify water leaks from pipelines carrying both water that is safe for human use and sewage water to reduce the public health risk and prevent structural damage to buildings—as the presence of fractured pipes is considered to be an engineering and environmental hazard. In addition, to distinguish between different underground pipe types—especially metal and PVC pipes, with and without leaks in the study area—a GPR system with a 600 MHz antenna frequency and various simulation modeling was used. Furthermore, we aimed to find a solution and accurately detect the exact location of the different pipes within the leak areas. By using this capability, we can effectively manage and maintain the pipes, leading to enhanced safety and efficiency.

1.1. Study Area

The study area in this study is located in a part of the El Hammam area on the northwestern coast of Egypt. It is positioned west of Alexandria and parallel to the Mediterranean coast. The boundaries of the study area are marked by longitude 29°21′45″ to 29°22′30″E and latitude 30°53′05″ to 30°53′30″N, as shown in Figure 1. Numerous paved roads, including the Alexandria–Matruh and El Hammam–Burg El Arab Roads, intersect the area. The area has a sequence of calcareous ridges and depressions that vary in altitude.

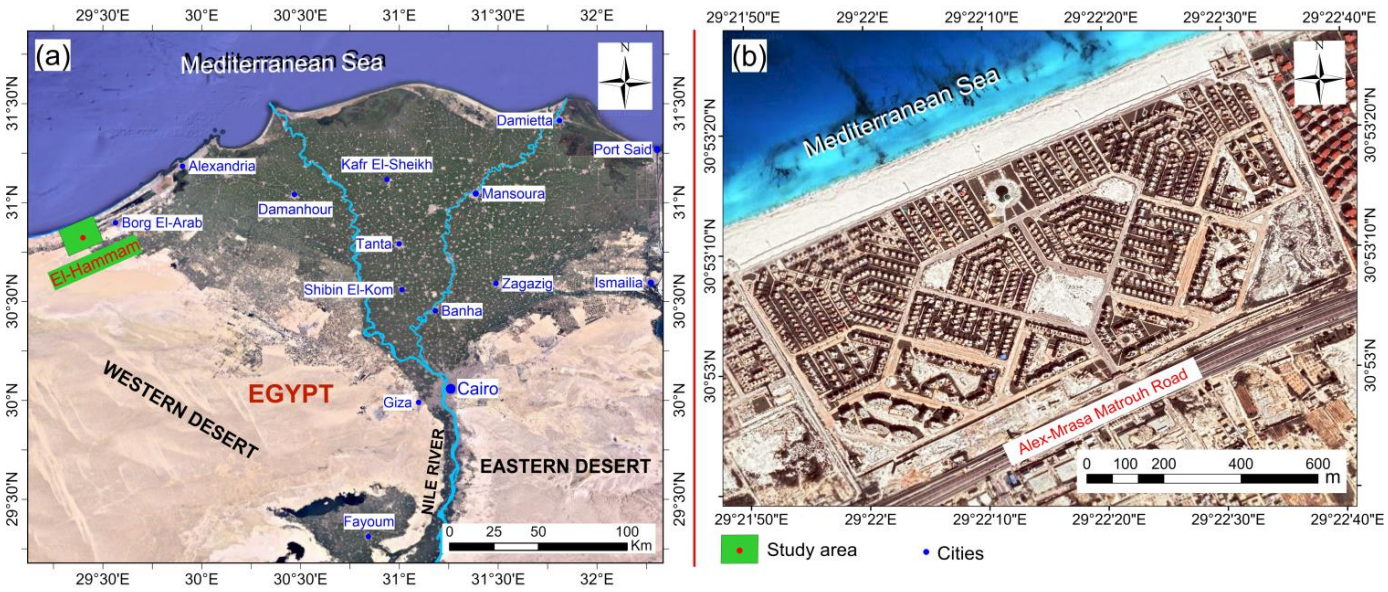

Figure 1. Google Earth map of Egypt showing the location of Egypt's landmarks (**a**). Enlargement of the study area (**b**).

The research area had extensive water seepage at the surface, as shown in Figure 2, which has caused environmental deterioration. Additionally, the water seepage has caused engineering problems, such as the cracking and tilting of some buildings. Furthermore, the residents are experiencing certain illnesses due to the mixture of portable and sewage water during water transportation from the source to the consumer.

Figure 2. Presence of water leaks on certain surface areas.

1.2. Geological and Geomorphological Setting

The surface geology of the study area is predominantly composed of Quaternary deposits, specifically Pleistocene oolitic calcareous ridges consisting of detrital oolitic limestone sediments, as indicated by satellite images, field observations and measurements, and literature sources [42,43] (as illustrated in Figure 3a). The oolitic limestone sediments are mainly composed of whitish layers of oosparite with a detrital texture, as shown in Figure 3b. Additionally, while conducting measurements during our field observations, we observed that certain regions contain sandy soil with depths ranging from one to two meters.

Geomorphologically, the majority of the study area is occupied by the coastal plain, based on information from various sources, such as satellite images, topographic maps, geologic maps, and field observations [42,44–46]. This coastal plain is characterized by a series of ridges separated by depressions, as shown in Figure 3c. These ridges comprise oolitic limestone from the consolidation of beaches and ancient dunes along the shoreline [42,46]. These formations are arranged in a south-to-north sequence [44,45] as follows: El Hammam depression, Gabal Maryut ridge (third ridge), Mallahet Maryut depression, El Max-Abu Sir ridge (second ridge), foreshore depression, and coastal ridges (first ridge). To obtain further information regarding Egypt's northwestern coast's geological and geomorphological setting, refer to the following sources: [44,47].

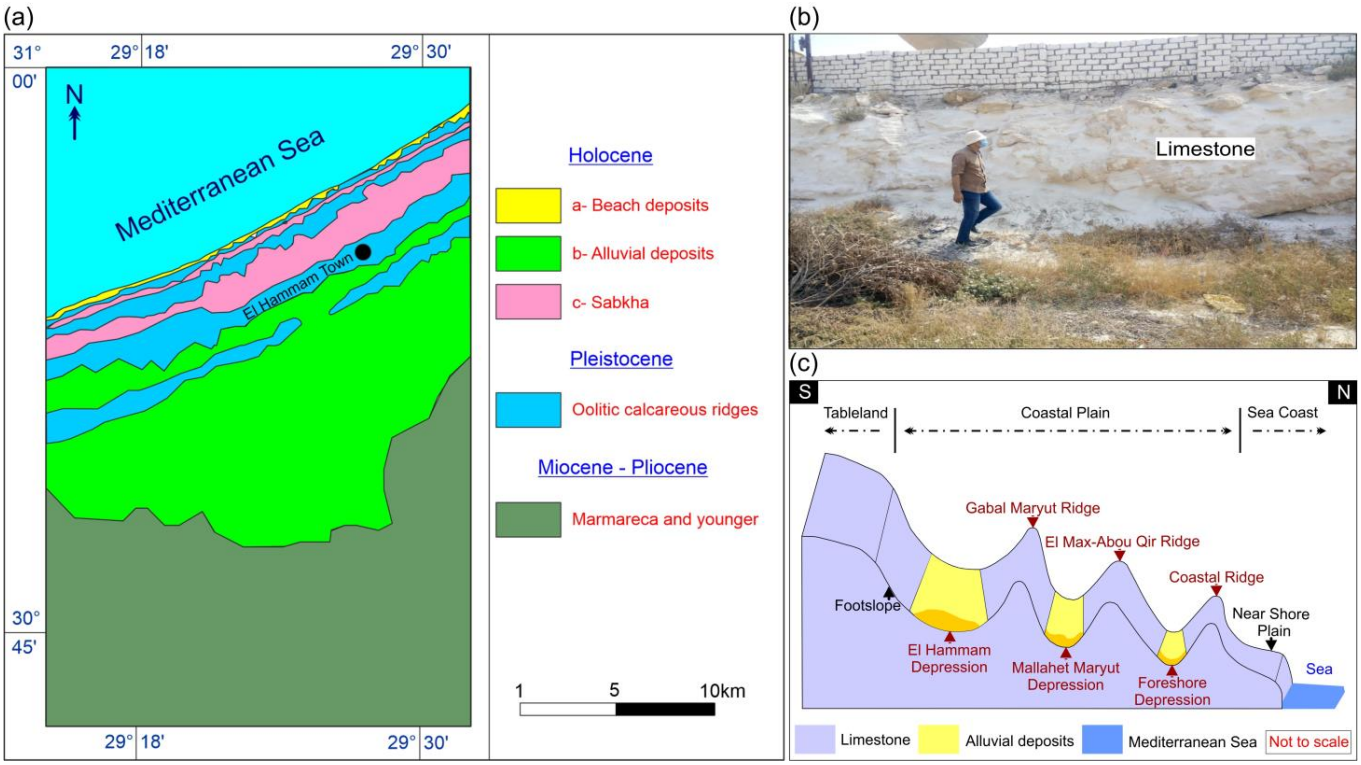

Figure 3. Geological map of the study area (modified after [42,43]) (**a**). Exposed limestone outcrops cover the study area (**b**). Geomorphologic units of the study area (modified after [45]) (**c**).

2. Materials and Methods

The GPR method uses short high-frequency electromagnetic (EM) pulses ranging from 10 MHz to 2.6 GHz [48], sent into the subsurface by a transmitter antenna and received by a receiver antenna to produce visual representations of shallow soil and rock conditions [49,50]. GPR works effectively in soils with low conductivity and can conduct quick and continuous scans over a large area within a short duration [51]. The depth penetration and resolution depend on the antenna frequency used. Higher frequencies provide a higher resolution but shallower depth penetration, while lower frequencies provide deeper penetration but with a lower resolution [52,53].

The magnitude of the reflected signal increases at an interface below the surface when there is a notable discrepancy in the physical characteristics of the two materials, resulting in a higher amplitude reflected wave that could be detected with GPR [54]. The physical properties of materials that affect subsurface wave propagation at GPR frequencies are conductivity (σ) measured in mS/m and dielectric constant (ε), which is dimensionless [55,56]. When the GPR emits electromagnetic waves into the ground, the receiving antenna records the variations in the return signal caused by encountering buried objects or boundaries between materials with different permittivities (Figure 4). The greater the change in permittivities of the medium, the stronger the intensity of the reflected wave, resulting in more apparent features on the GPR image [9].

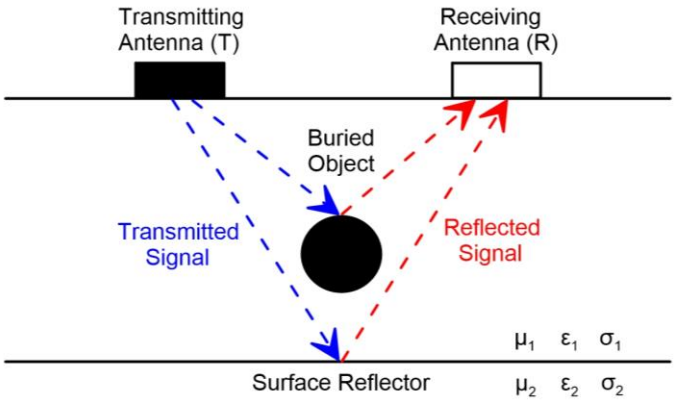

Figure 4. The propagation of EM waves in subsurface materials (Modified after [57]).

A GPR survey was conducted in a specific area of El Hammam town on the north-western coast of Egypt. It was most likely carried out to identify and map the leak areas and the pipes responsible for these leaks to facilitate maintenance and better understand their properties, enabling a more convenient distinction between them.

Twenty-two GPR profiles were conducted at different locations in the study area using the time mode for data contact acquisition (Figure 5) via the RIS Hi-MOD-IDS georadar system. The system operates by keeping the transmitter and receiver at a constant distance while moving along a profile to collect the data. It consists of a monitor or external PC, a control unit with a 32-bit processor, two shielded antennas (transmitter Tx and receiver Rx) with a dominant frequency of 600 MHz, a battery, and a measuring wheel (as shown in Figure 6). The transmitter generates short-period, high-voltage pulses; these pulses are transmitted to the transmitting antenna (Tx), which emits them into the ground. The studied signals of the materials are gathered by the receiving antenna (Rx), amplified, preliminarily processed by the control unit, and formatted to display the field data on the external PC [58].

Figure 5. Location map of the GPR profiles in the study area.

Figure 6. RIS Hi-MOD-IDS georadar system (**a**) and field photographs during the GPR data acquisition (**b**,**c**).

The raw data from the GPR profile was adjusted for corrected positioning and subjected to various filters to enhance the subsurface reflections during post-processing using the Reflex software v.9.5. Reflex software is used to obtain a more precise image with better brightness and contrast, and to eliminate any noise in the data. This software aided in interpreting the data by transforming the raw data into a 2D format. The objectives of post-processing primary data were achieved through several goals, including improving the signal-to-noise ratio, removing any irregularities induced by the system, and correcting any geometric effects caused by data acquisition [59]. We applied the following six post-processing steps to our data to detect the leak areas on the radar section.

1. Time-zero correction is the first step in processing GPR data, which involves adjusting traces to a common time-zero position [57]. This correction is necessary due to factors such as thermal drift, electronic instability, cable length differences, and variations in the antenna air gap, which can cause "jumps" in the air/ground wavelet's first arrival time [60].
2. Dewow filtering is a common processing step that uses temporal filtering to remove the data's DC signal and low-frequency components, resulting in a mean zero level [61].
3. Background removal is a frequently used step in GPR data processing that involves applying a high-pass filter or average trace removal as a form of spatial filtering. This technique helps to eliminate background noise and enhance weaker signals to become

more visible in the processed section. In this process, the mean of all traces in a section is calculated and subtracted from each trace, which is particularly useful for reducing antenna ringing [61].

4. Gain (energy decay) is one of the processing steps applied to GPR data. In subsurface exploration using radar signals, it becomes harder to distinguish events at greater depths due to rapid signal attenuation [61]. So, this step aims to enhance later arrivals by compensating for the energy loss that occurs during signal propagation through the subsurface, such as spherical divergence and intrinsic and scattering attenuation [62].
5. Band-pass filtering (Butterworth) is commonly used to eliminate noise caused by human or system interference and enhance the visual clarity of GPR data (e.g., the removal of high-frequency "speckle" from radio transmissions or the striping effect from antenna ringing [60,62]). It consists of a combination of high-pass and low-pass filters that allow frequencies on either side of the peak frequency of the transmitted signal to pass through [63].
6. Time-to-depth conversion is an important processing step for realistic interpretations and elevation corrections of GPR data. It is necessary to convert two-way travel time to depth in the GPR sections to help determine the target's depth. This step requires an accurate estimate of the subsurface velocity, which can be obtained through ground-truthing, common midpoint surveys (CMPs), or hyperbolic velocity analysis [62]. This study used the constant velocity based on ground truthing, precisely 0.12 m/ns, to account for limestone outcrops in the study area [64].

Subsequently, two processing steps were employed using designed MATLAB® codes to distinguish between pipe materials and determine their type, as below:

1. Envelope is a technique that enhances the signal-to-noise ratio of data by processing the data in a way that allows incoherent stacking. This method involves squaring and adding the actual measured antenna voltage and its quadrature, which is equal to the magnitude of the Hilbert transformation of the radar trace. To implement this method, one can sum the squared radar trace data and their squared numerical differences, which is a simple and efficient approach. This is because the differential or integral of a sinusoid can be represented as a phase shift of $\pi/2$. The ultimate goal of this processing step is to generate a scattering amplitude envelope that represents the average amplitude of scattering versus depth [65]. The signals received by the GPR antenna are often complex, with various reflections arriving at different times due to different subsurface materials and features. The envelope technique extracts the maximum amplitude of these received signals over time. GPR signals typically contain both positive and negative peaks due to reflections. By taking the absolute value of the signal, the negative peaks become positive, resulting in a rectified version of the signal. The maximum values (peaks) of this rectified signal are extracted over a specific time range to create an "envelope" of the original signal. This processed signal can provide a clearer image of the subsurface structures than the raw GPR data. So, we designed a simple code to perform this step, which involved gathering the positive and negative reflections. This process effectively amplified the amplitude reflection for each pipe material, enabling us to identify the type of these pipes.
2. Migration is a processing technique that is typically used to enhance section resolution and produce more accurate subsurface images in GPR. It is considered to be the most contentious of all GPR processing techniques. As the waves received by the GPR antenna are typically acquired vertically along the acquisition line, they do not accurately represent the positions of small-scale diffractors or sloped reflectors. This processing step extends the recorded wavefield downward to its origin to capture these features and move the hyperbola signal to the focal position more accurately [52,62]. The F-K migration technique converts hyperbola signals to object's locations using a constant velocity [66]. This approach uses the exploding source model, which assumes that the scattered signal field originates from an explosion at the object's location. It operates on frequency and wavenumber in the Fourier domain and then inverses to the time

domain [67]. After applying the time-to-depth conversion processing step, we applied this step to the simulated and field data. We designed a basic code derived from the F-K migration code to improve the positioning of reflection points and create a more accurate representation of the subsurface features. The migration process enhanced the visibility of pipeline reflections, making them more discernible, particularly within the leak areas that remained undetectable in the radar cross-section derived from the field data after post-processing. Finally, we could deduce the probable pipeline material type and its precious position by comparing the reflection characteristics with known material signatures.

3. Results

The study utilized two types of radar profile data: the FDTD simulation radar profile and the radar profile obtained from fieldwork conducted in a specific area suspected of water leaks using a GPR instrument. The FDTD simulation data were produced using MATLAB® software v. R2016b, incorporating specific parameter settings for the leaky water pipe scene. The simulation aimed to utilize signature fingerprints to identify metal and PVC pipes and detect areas of leaks in the measured radar sections. Henceforth, it aimed to minimize uncertainties and prevent misinterpretation. The electrical property information, such as relative dielectric permittivity (ε_r), magnetic permeability (μ), and electrical conductivity (σ), for each testing parameter was gathered from the relevant literature. Subsequently, the GprMax electromagnetic simulator, integrated with MATLAB®, was utilized to generate a comprehensive set of radar profiles, both with and without leak conditions. These profiles were created based on the assumption that the backfill soil materials were homogenous under ideal conditions.

3.1. Simulated GPR Image

To demonstrate the effectiveness and applicability of GPR in detecting concealed water leak areas and distinguishing between various hidden pipe materials, two simulation images were generated using the GprMax simulator for two different conditions.

The GPR images simulated using GprMax v.3.0.0b20 employed a Hertzian dipole source with a Ricker waveform featuring a center frequency of 600 MHz. The source was positioned at a distance of 0.4 m and a depth of 0.2 m, while a receiver was placed at a distance of 0.5 m and a depth of 0 m. The transmitter source and the receiver were incrementally moved by a distance of 0.03 m for each step. The simulations employed a relative magnetic permeability, set to 1. Figure 7a,b illustrate the diagrams corresponding to simulation models 1 and 2, respectively. Models 1 and 2 had dimensions of 4 m in length and 4 m in depth. Both models possessed an initial layer of air with a relative permittivity of 1 and a conductivity of 0 S/m. The second layer in both models represented sandy soil, characterized by a relative permittivity of 5 and a conductivity of 0.00001 S/m. The third layer in both models represented a limestone layer, possessing a relative permittivity of 6 and a conductivity of 0.0005 S/m.

Moreover, in Model 2, two additional layers were introduced: one consisting of water-saturated sand and another comprising water-saturated limestone. These water-saturated layers exhibited relative permittivity values of 30 and 8, respectively, and conductivity values of 0.001 and 0.002 S/m, respectively. Both models included two targets: a metal pipe (represented as a blue circle), located at a distance of 1.5 m, and a PVC pipe (represented as a green circle), positioned at a distance of 2.7 m. Both targets were at a depth of 1 m, with a diameter (Ø) of 0.32 m and a cross-sectional area of 0.08 m^2.

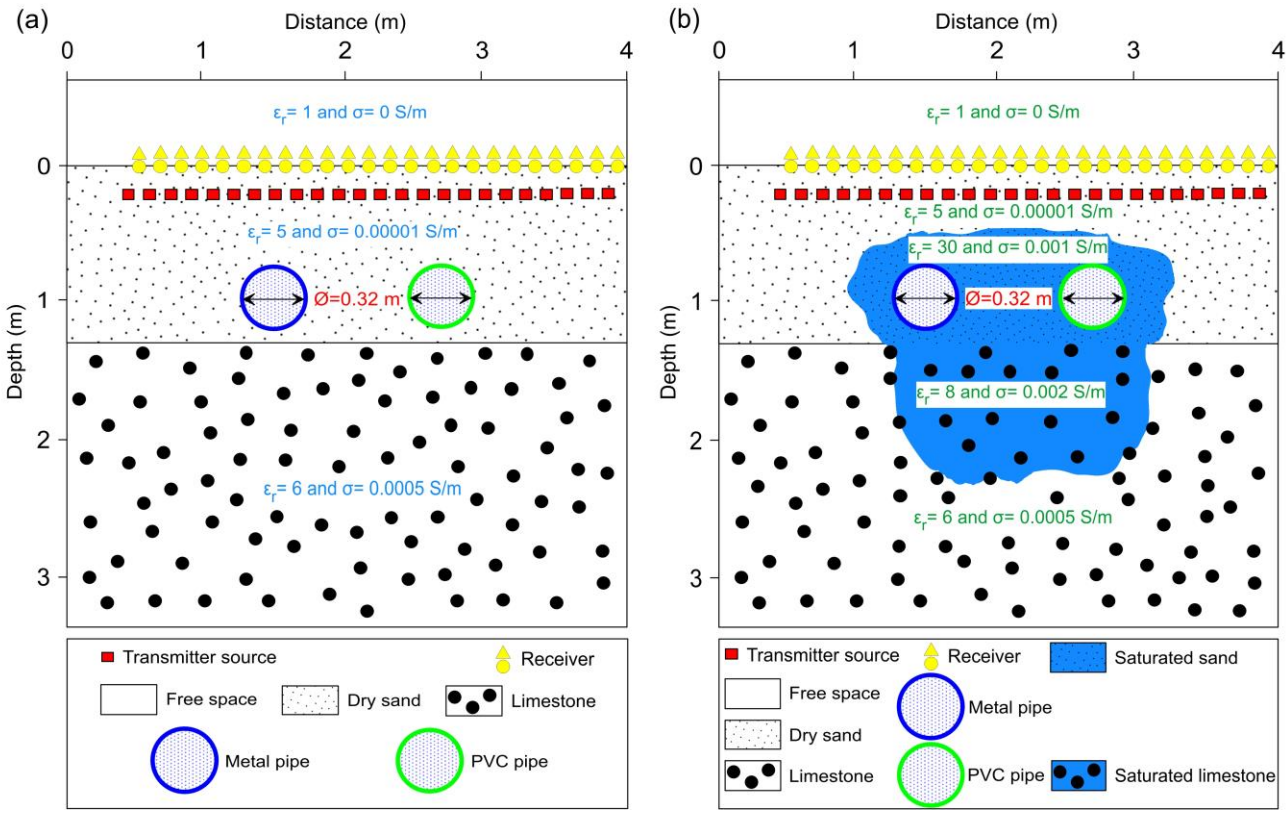

Figure 7. GprMax simulation models for dry condition (**a**) and water leak condition (**b**).

The model's parameters were normalized to obtain the simulated GPR image, as displayed in Figure 8a,b. The simulated time window was set to 35 ns, and B-scan measurements were obtained with a spatial and time step of 0.01 m and 0.038 ns, respectively. Figure 8a,b present the most favorable outcomes of the simulation, serving as evidence for the usability and capability of GPR in detecting these invisible water leak pipes. Using Matlab®, we successfully subtracted the influence of the direct wave effects from the figures to accurately detect metal and PVC pipes in dry and leak areas. The examination of Figure 8a,b revealed that the reflection characteristics of intact metal or PVC pipes could be easily distinguished. However, differentiation became challenging when dealing with leaky metal or PVC pipes. This difficulty arose due to the presence of saturated or wet soil causing additional reflections, disrupting the characteristic hyperbolic or V-shaped signature of metal and PVC pipes in the radar profile. These findings confirmed that GPR holds significant potential as a valuable investigative tool for detecting areas of pipe leaks. Moreover, it demonstrated an adept ability to easily distinguish between the different pipe materials within the dry areas, yet encounters challenges when applied in the leaky areas.

To further emphasize the challenge of being unable to detect the reflection patterns of metal and PVC pipes in the leaky areas, we applied F-K migration analysis to the simulated GPR image, as illustrated in Figure 9a,b. This analytical technique enhanced the interpretation and identification of metal and PVC pipes, improving the ability to detect the metal and PVC pipes within dry and leaky areas at their precise position and depth. The simulated data can be spatially matched as a fingerprint with real-world measurements by performing data migration, allowing for a more precise comparison and analysis.

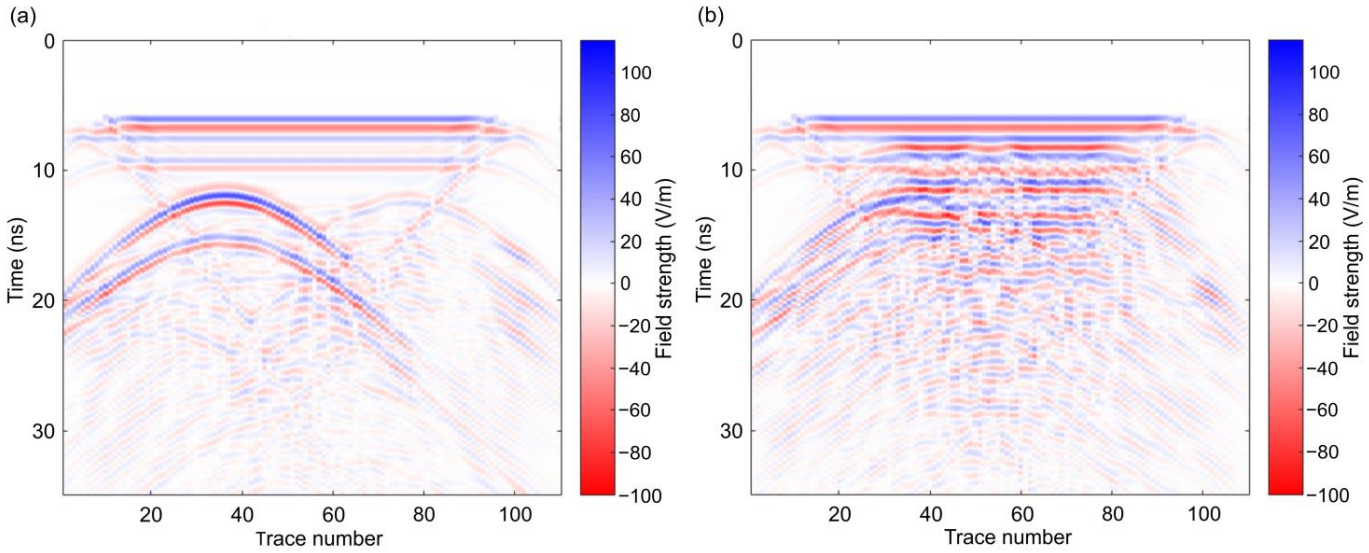

Figure 8. Simulated GPR images from a dry model (**a**) and a water leak model (**b**).

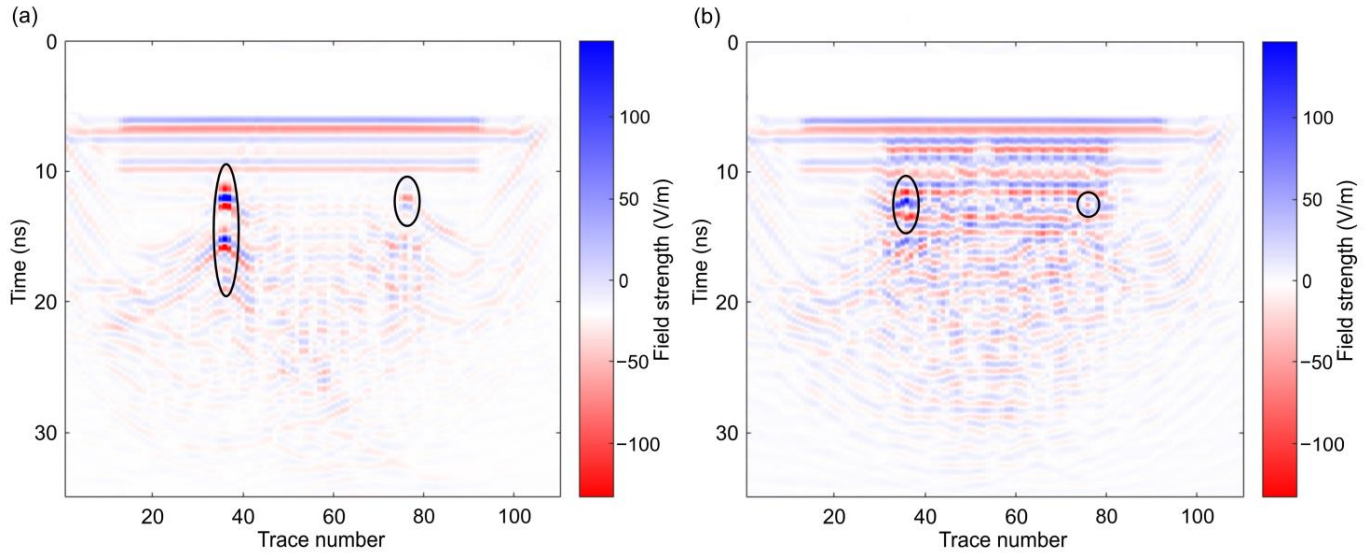

Figure 9. Migrated GPR images from a dry model (**a**) and a water leak model (**b**), noting that the black circles indicate the metal and PVC pipes.

In Figure 8a, the identification of metal and PVC pipes within dry soil is straightforward. However, in the model of saturated soil, as is shown in Figure 8b, the accurate detection of these pipes became challenging due to the alteration of their reflective properties induced by pipe leaks. In contrast, the results presented in Figure 9a exhibit a notable improvement after the migration process. This enhancement enabled the precise localization and depth determination of metal and PVC pipes within dry soil. Furthermore, in Figure 9b, the improved outcomes are particularly evident when dealing with saturated soil, distinct from those seen in Figure 8b. In this case, the metal pipe's position and depth can be readily identified. While the PVC pipe detection was slightly less noticeable than the metal pipe, it remained discernible. It is worth noting that the diminished reflection of the PVC pipe ariose from its considerably lower permittivity compared to the surrounding saturated soil. However, alternative methodologies employed in this study could effectively detect the PVC pipe under these conditions.

3.2. Real GPR Image

3.2.1. Detection of Leak Areas

The conventional method used to detect anomalies, including hyperbolic reflections, differences from normally smooth reflection patterns, and signal frequency changes, is radar data analysis. Hyperbolic reflections are produced by point reflectors such as pipes, rocks, or voids in the ground. Frequency changes in radar signals result from modifications in the dielectric properties of the medium through which the signals travel. The presence of water saturation, for example, reduces the frequency and concentrates the beam width of the radar signal.

According to [68], there is a significant difference in the dielectric properties of water and soil. As a result, radar reflections appear more prominently in wet areas against a background of dry soil. The high radar reflection zone can also be used to delineate the extent of the wet soil. Figures 10 and 11 demonstrate that the wet soil area displayed a higher radar intensity than the surrounding dry soil in the study area. The profiles obtained using the 600 MHz antennas demonstrated a penetration depth of approximately 3.5 m at 50 nanoseconds, with a velocity of approximately 0.12 m per nanosecond. Table 1 shows the extension of each leak area along the mentioned profiles.

Table 1. The size or extension of the leak areas located in the study area.

Profile Number	Leak Areas	Distance (m)		Depth (m)	
		Start	**End**	**Start**	**End**
P(1)	1st	18.6	20.1	0.4	1.6
	2nd	24	27.6	0.4	1.6
P(2)	1st	19.5	21.9	0.4	1.3
	2nd	41.8	46.1	0.4	1.96
P(8)	1st	106.2	107.8	0.4	1.64
P(11)	1st	29.4	31	0.4	1.64
P(15)	1st	9.2	11.2	0.4	1.4
	2nd	15.6	17	0.4	2.2
	3rd	117.4	124.2	0.4	3.2
P(17)	1st	77.1	78.2	0.44	1.32
	2nd	82.6	84.6	0.44	1.62
P(18)	1st	2.8	6.2	0.4	2.44
	2nd	101.7	105.7	0.4	2.52
P(20)	1st	4.5	6.7	0.4	1.8
	2nd	8.5	11.7	0.4	2.9
P(21)	1st	25.3	30.1	0.2	2.44
	2nd	33.6	41.2	0.24	2.64
P(22)	1st	194.7	199.1	0.28	2.32

It can be stated that the damage to the fresh water and sewer pipes is responsible for these leak areas, which are frequently concentrated in the northeast and southeast regions, with some being dispersed throughout other parts of the study area.

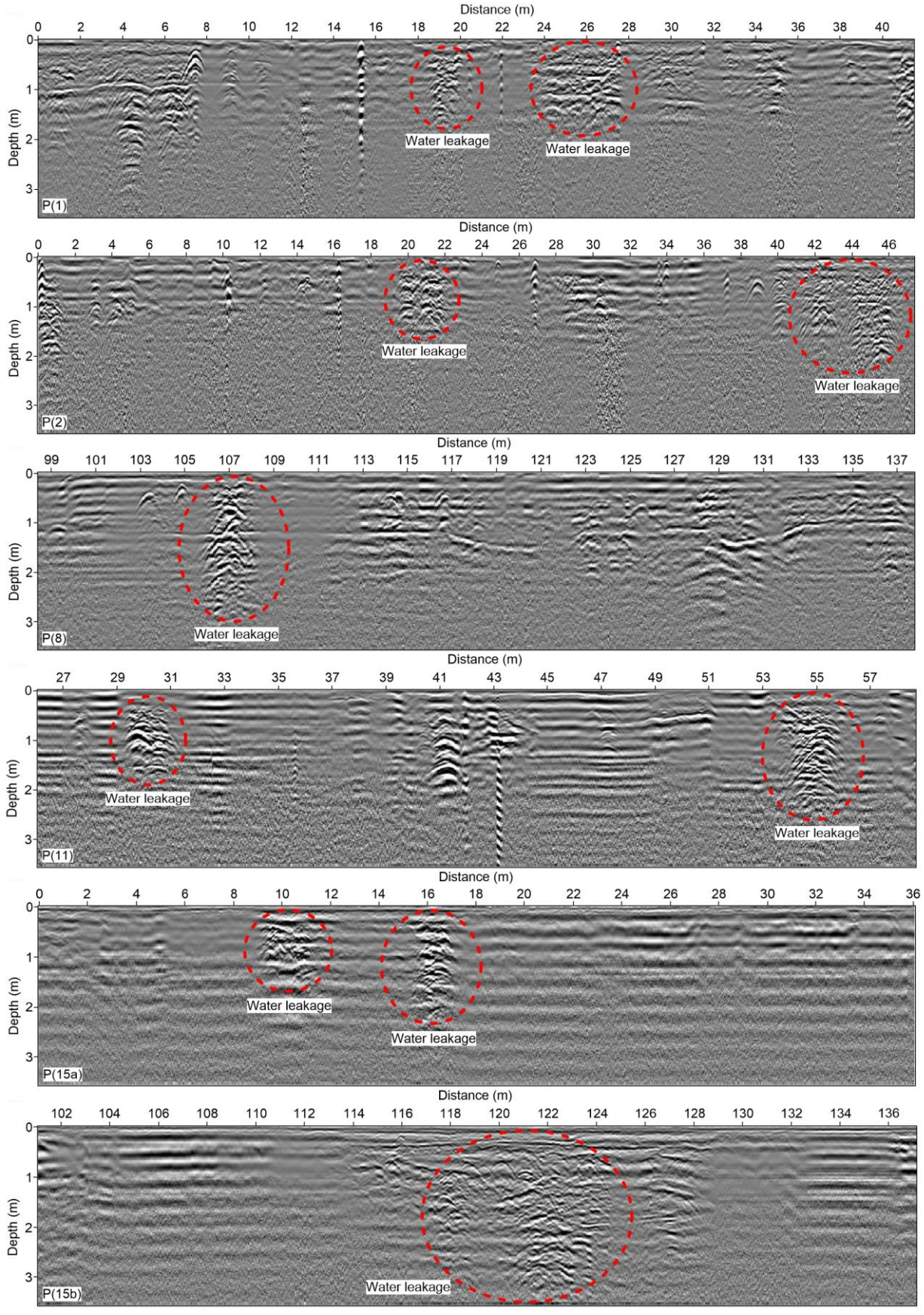

Figure 10. 2D GPR sections showing the water leaks in profiles 1, 2, 8, 11, and 15 within the study area.

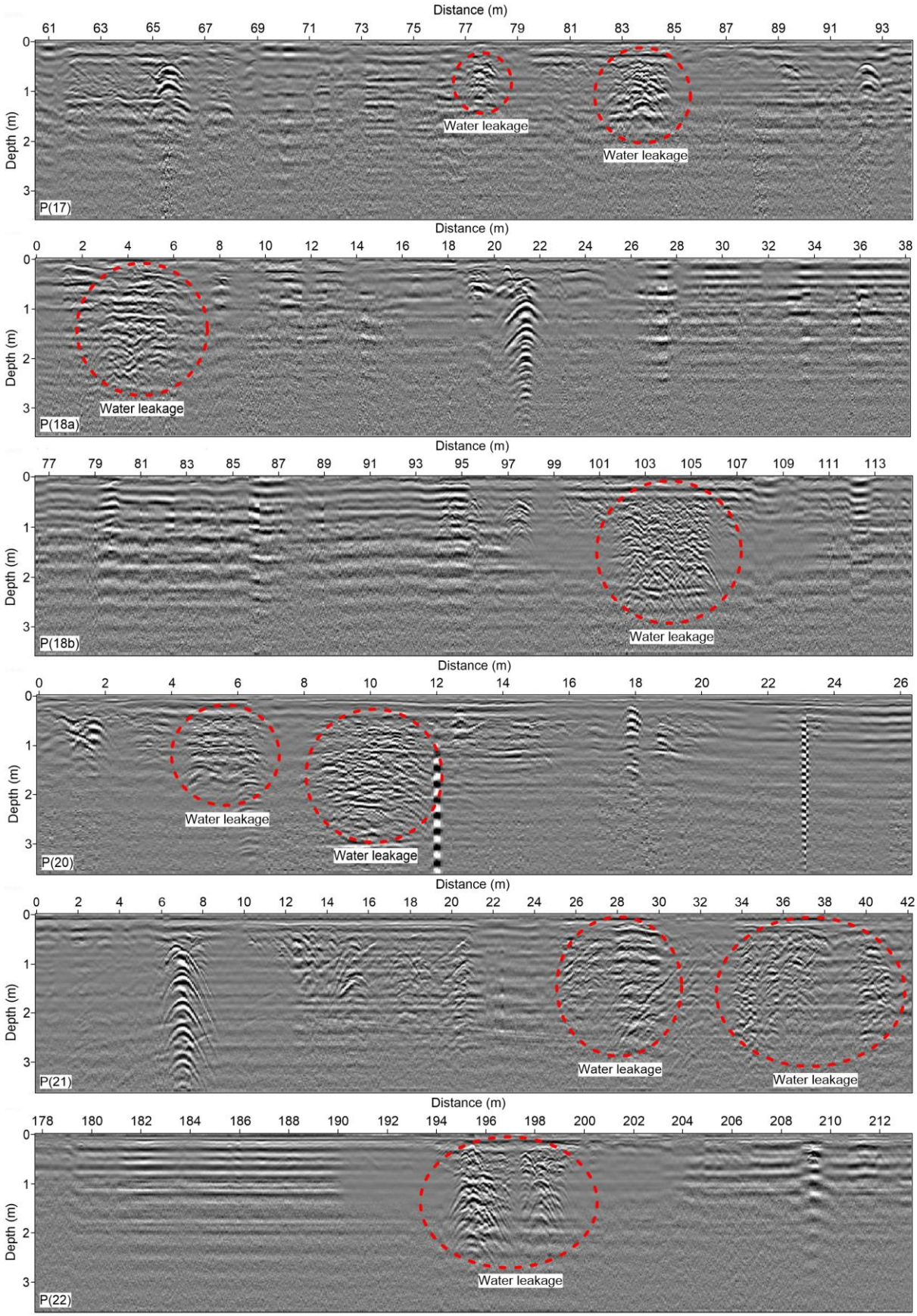

Figure 11. 2D GPR sections showing the water leaks in profiles 17, 18, 20, 21, and 22 within the study area, continued.

3.2.2. Differentiation between Pipe Materials

- Using trace and radar section analysis

GPR surveys can successfully detect underground utilities, including metallic and non-metallic pipes. These utilities typically appear as hyperbolas in response, with metallic pipes exhibiting high dielectric contrast to soil, resulting in a prominent appearance in the GPR profile. On the other hand, non-metallic utilities such as PVC pipes are less noticeable. The size of the hyperbola varies depending on the size of the pipes. The length of the top part of the hyperbola is similar to the perimeter of the semicircle of the pipe when viewed in the GPR cross-section.

Figures 12–15 show the trace and radar sections for some selected profiles within the study area.

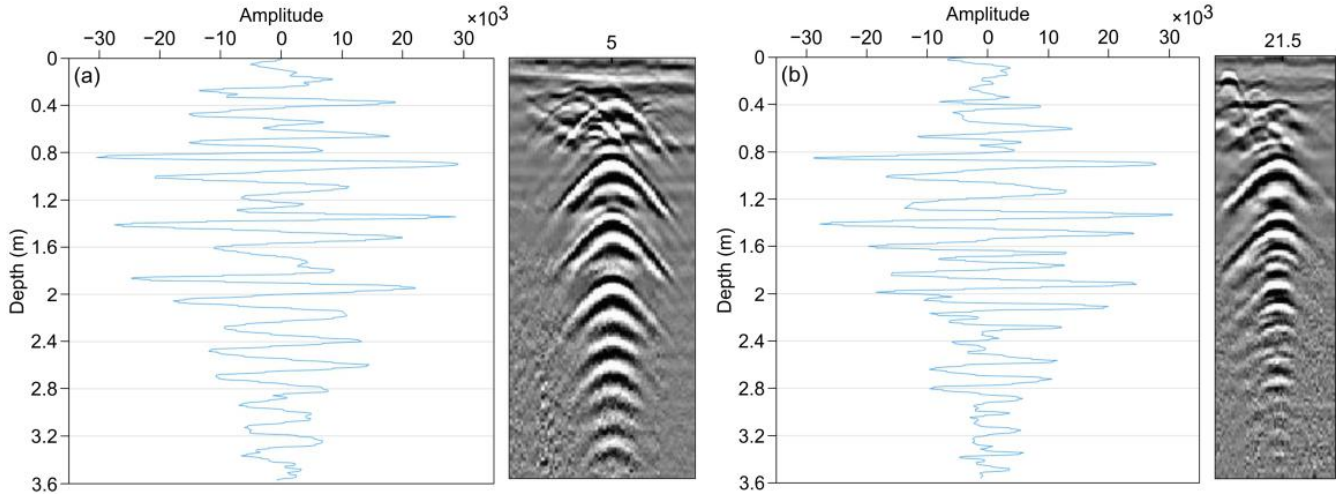

Figure 12. The amplitude and hyperbolic shape of metal pipe without leaks along some traces and the corresponding radar sections of profiles 16 (**a**) and 18 (**b**).

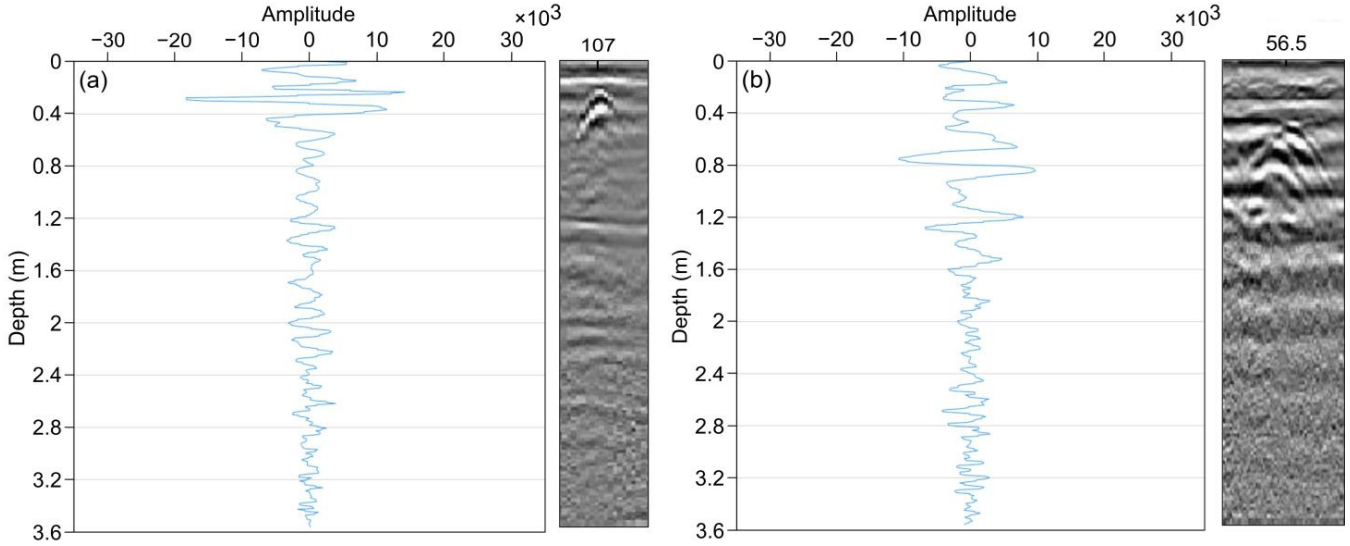

Figure 13. The amplitude and hyperbolic shape of PVC pipe without leaks along some traces and the corresponding radar sections of profiles 8 (**a**) and 18 (**b**).

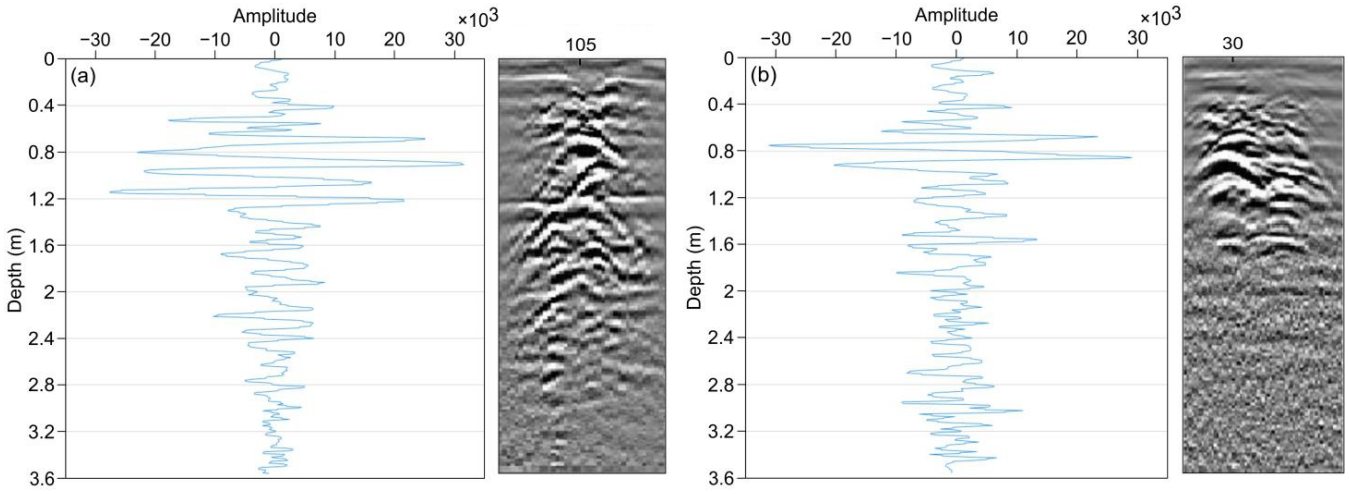

Figure 14. The amplitude and hyperbolic shape of metal pipe with leaks along some traces and the corresponding radar sections of profiles 8 (**a**) and 11 (**b**).

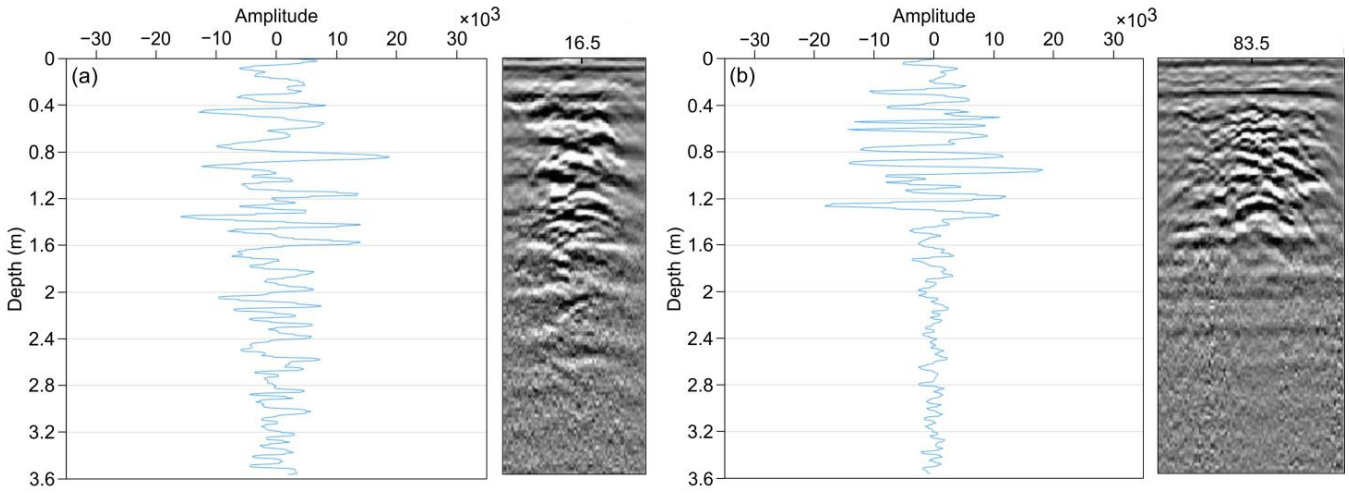

Figure 15. The amplitude and hyperbolic shape of PVC pipe with leaks along some traces and the corresponding radar sections of profiles 15 (**a**) and 17 (**b**).

Figure 12a,b display an amplitude of reflection range of approximately 30 to −30 in the trace section. This generated large hyperbolas in the corresponding radar section, indicating the presence of a metal pipe.

Conversely, Figure 13a,b exhibit an amplitude of reflection range of approximately 10 to −10 in the trace section, causing a small hyperbola to appear in the radar section. This hyperbola suggests the presence of a PVC pipe.

Figure 14a,b show an amplitude of reflection range of approximately 30 to −30, with additional parts ranging from 10 to −10 in the trace section. This generated a large hyperbola with low to moderate radar reflection in the radar section. The hyperbola with low to moderate radar reflection was especially conspicuous compared to the surrounding area's dry soil, signifying a metal pipe with leaks.

On the other hand, Figure 15a,b present an amplitude of reflection range of approximately 10 to −10, with additional segments ranging from 10 to −10 in the trace section. This generated a small hyperbola with low to moderate radar reflection in the corresponding radar section. The hyperbola with low to moderate radar reflection was notably conspicuous when compared to the dry soil in the surrounding area, indicating the presence of a PVC pipe with leaks.

Figures 12–15 represent some examples of different pipes with and without leaks within the study area, which revealed that metal pipes—with or without leaks—displayed a significant amplitude of reflection compared to PVC pipes. A metal pipe in the medium caused a considerable variation in the dielectric constant, resulting in a strong reflection of radar signals; thus, explaining the reason for the prominent appearance of the metal pipes as a large hyperbola in the GPR cross-section. While PVC pipes are mostly transparent, the presence of air or water in the pipe reflected radar signals, resulting in a weak hyperbola in the GPR cross-section. The trace section offered an advantage in distinguishing between metal and PVC pipes within the water leak areas. In contrast, the radar section failed to differentiate between them, as shown in Figure 14b. Based on the findings illustrated in Figures 12–15, it was evident that the radar section identified metal and PVC pipes effectively within dry areas. However, the radar section struggled to detect and distinguish between these pipes in leaky areas. Trace analysis, on the other hand, offered a solution to this challenge. By demonstrating the amplitude reflection of the metal and PVC pipes within leaky areas, trace analysis proved to be more effective compared to radar analysis. This advantage positioned trace analysis as a superior method for addressing this particular challenge.

- Using envelope and F-K migration analysis

Two MATLAB® codes were used to perform envelope and F-K migration analyses on the GPR data. The purpose was to easily differentiate between metal and PVC pipes within the study area and attempt to detect their accurate position under various leaky conditions. The envelope determination process involves applying energy-based attribute analysis, as discussed by the authors in [69]. It is worth noting that the GPR envelope is closely associated with the electric impedance [52]. A solution to the migration problem was presented using a formal wave equation solution using Fourier transforms [66]. Figures 16–19 compare the metal and PVC pipes with and without leaks through the original radar, enveloped, and migrated sections.

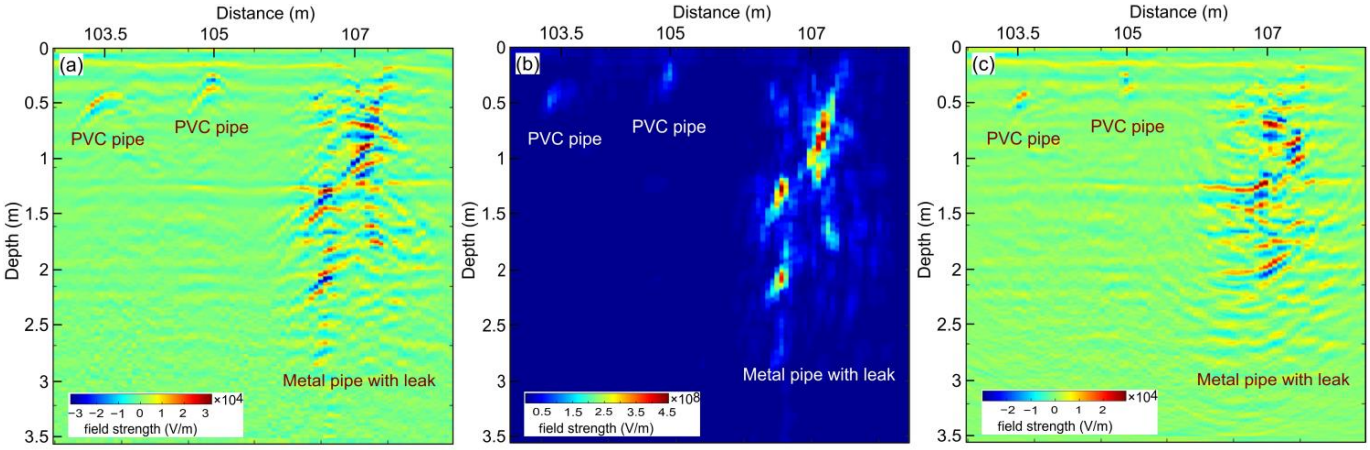

Figure 16. The reflection of metal and PVC pipes with and without leaks along the radar (**a**), enveloped (**b**), and migrated (**c**) sections of profile 8.

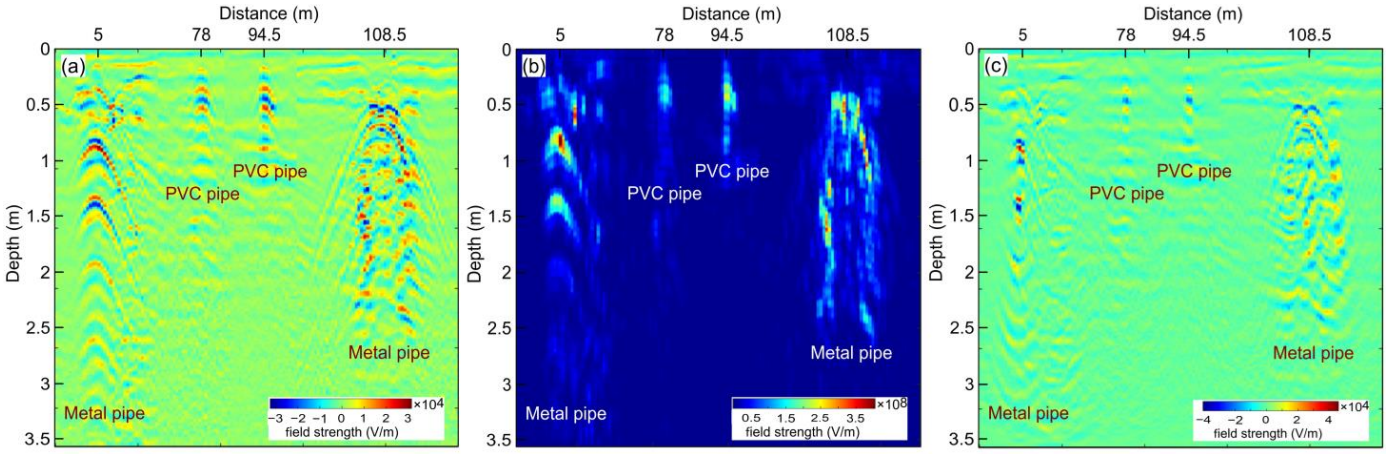

Figure 17. The reflection of metal and PVC pipes with and without leaks along the radar (**a**), enveloped (**b**), and migrated (**c**) sections of profile 9.

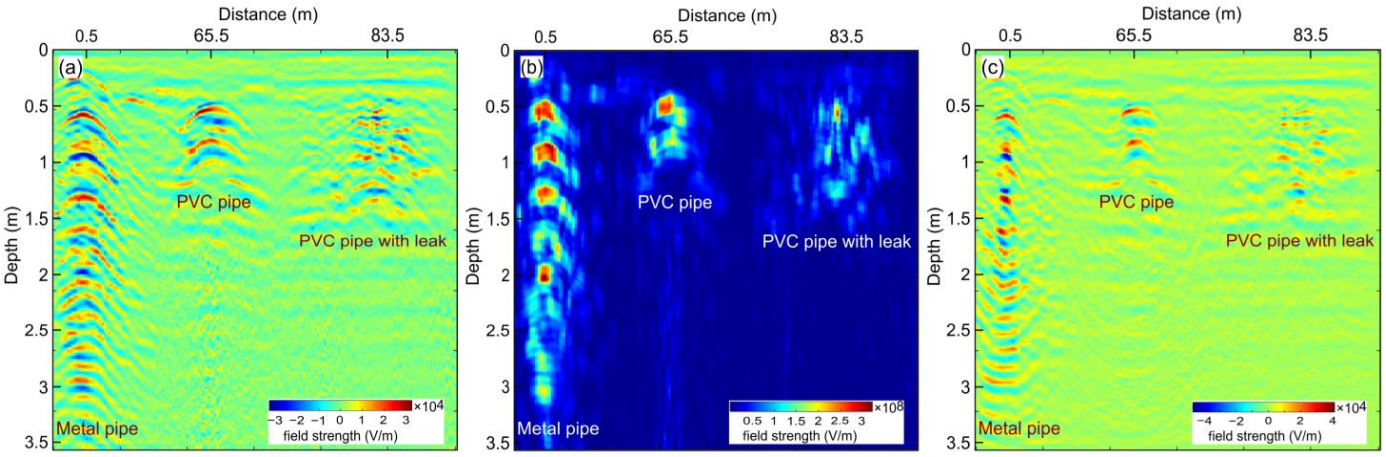

Figure 18. The reflection of metal and PVC pipes with and without leaks along the radar (**a**), enveloped (**b**), and migrated (**c**) sections of profile 17.

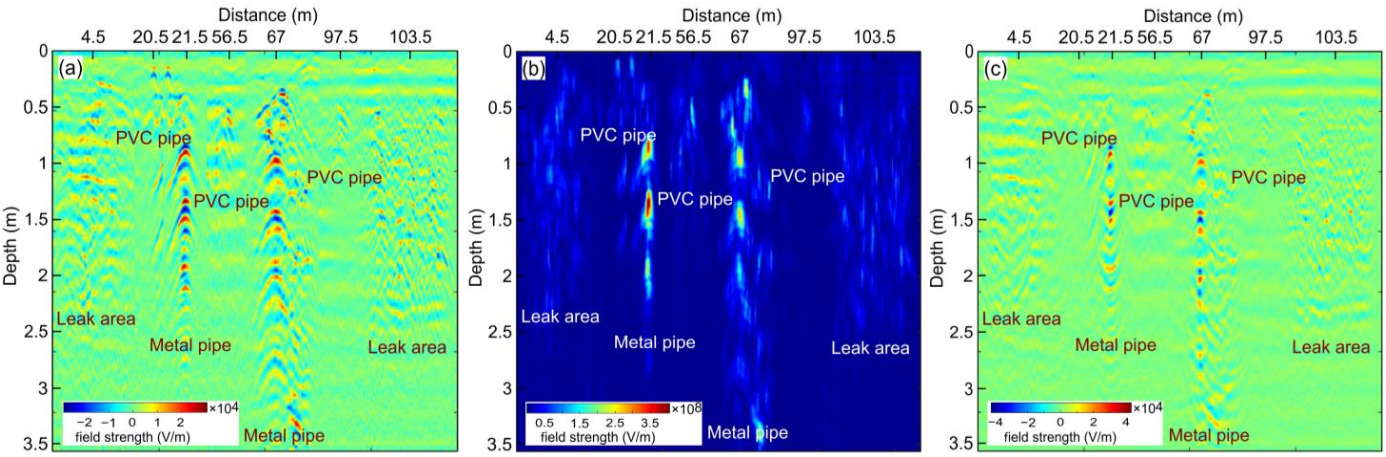

Figure 19. The reflection of metal and PVC pipes with and without leaks along the radar (**a**), enveloped (**b**), and migrated (**c**) sections of profile 18.

Figure 16a displays a radar section—a simple interpretation that revealed the presence of two PVC pipes as indicated by two small hyperbolas at distances of 103.5 and 105 m,

and a metal pipe with leaks identifiable by one large hyperbola, whereby high radar reflectivity contrasted against the dry soil in the surrounding area at a distance of 107 m. The GPR data, shown in Figure 16b, were subjected to energy attribute analysis using the Hilbert transform to determine the instantaneous amplitude (envelope). Following this procedure, the characteristic hyperbolic form, including the positive and negative peaks, was transformed into a singular positive peak concentrated within a specific region. The provided illustration shows two low-amplitude reflections at distances of 103.5 and 105 m, illustrating the presence of two PVC pipes.

Furthermore, one high-amplitude reflection with some areas of low-amplitude reflection was observed at a distance of 107 m, indicating the presence of a metal pipe with leaks. Meanwhile, Figure 16c presents outcomes derived from the F-K migration process, revealing that the metal and PVC pipes are now accurately positioned. Notably, a distinct contrast was observed between the two PVC pipes situated at distances of 103.5 and 105 m, exhibiting through smaller dots with a lower color amplitude. In contrast, the metal pipe with a leak displayed a higher color amplitude at a distance of 107 m.

Figure 17a on profile 9 presents a radar section revealing the presence of two PVC pipes as indicated by the two small hyperbolas at distances of 78 and 94.5 m, and two metal pipes identifiable by two large hyperbolas at distances of 5 and 108.5 m. Figure 17b shows the enveloped section after being subjected to the energy attribute analysis. This analysis demonstrated that, following the conversion of both positive and negative peaks into a single positive peak within a specific region, two low-amplitude reflections were visible at distances of 78 and 94.5 m, indicating the presence of two PVC pipes. Additionally, two high-amplitude reflections were visible at distances of 5 and 108.5 m, indicating the presence of two metal pipes. Figure 17c illustrates the migrated section after undergoing the F-K migration process. The implementation of this procedure revealed the precise alignment of the metal and PVC pipes. Of significance was the evident disparity between the pair of PVC pipes positioned at distances of 78 and 94.5 m. This distinction became apparent due to the presence of smaller dots with a lower color amplitude. On the contrary, the two metal pipes exhibited a more pronounced color amplitude at distances of 5 and 108.5 m, highlighted by small multiple dots, creating a noticeable contrast.

Figure 18a depicts a radar section, revealing the presence of one metal pipe as identified by one large hyperbola at a distance of 0.5 m. Additionally, one small hyperbola was visible at a distance of 65.5 m, indicating the presence of a PVC pipe. Another small hyperbola with moderate radar reflectivity contrasted against the dry soil in the surrounding area at a distance of 83.5 m revealed the presence of a PVC pipe with leaks. Figure 18b shows the enveloped section after subjecting it to the energy attribute analysis. Upon completing this procedure, which involved consolidating the positive and negative peaks into one positive peak within a focused zone, it became evident that there was one high-amplitude reflection; this could be observed at a distance of 0.5 m, revealing the existence of a single metal pipe. Additionally, one low-amplitude reflection was visible at a distance of 65.5 m, indicating the presence of one PVC pipe. Finally, one low-amplitude reflection with some areas of low-amplitude reflection was visible at a distance of 83.5 m, indicating the presence of a PVC pipe with leaks.

Figure 18c illustrates the migrated section after undergoing the F-K migration process. Here, it is essential to highlight the noticeable difference displayed by a single metal pipe located at a distance of 0.5 m. This divergence was emphasized by the existence of compact dots extending downward with depth, characterized by a heightened color amplitude. Conversely, the presence of a PVC pipe became evident as indicated by a lower color amplitude at a distance of 65.5 m, marked by the presence of small dots. Furthermore, a lower color amplitude, coupled with some areas of even lower color amplitude, was observed at a distance of 83.5 m. This occurrence signified the presence of a PVC pipe with leaks, thus establishing a discernible contrast.

Figure 19a presents a radar section, which identified the presence of three PVC pipes identifiable by three small hyperbolas at distances of 20.5, 56.5, and 97.5 m. Furthermore,

the presence of two metal pipes was established as two large hyperbolas were detected at distances of 21.5 and 67 m. Additionally, two areas of low to moderate radar reflectivity contrasted against the dry soil in the surrounding area at distances of 4.5 and 103.5 m, indicating the presence of leak areas. Figure 19b displays the enveloped section after subjecting it to the energy attribute analysis. After this process, the distinct hyperbolic shape, encompassing its positive and negative peaks, was converted into a single positive peak, focused within a defined area. The illustration presented reveals the presence of three PVC pipes as identified by three low-amplitude reflections at distances of 20.5, 56.5, and 97.5 m. Furthermore, the existence of two metal pipes was evidenced by the presence of two pronounced reflections at distances of 21.5 and 67 m, which exhibited high amplitude. Finally, two regions with low to moderate amplitude reflection were visible at distances of 4.5 and 103.5 m, indicating the presence of two leak areas.

Figure 19c shows the migrated section after undergoing the F-K migration process. Upon implementing this procedure, it became evident that a distinction emerged between three lower color amplitudes at distances of 20.5, 56.5, and 97.5 m. These amplitudes were associated with three PVC pipes and represented by small dots. In contrast, two heightened color amplitudes at distances of 21.5 and 67 m signified the presence of two metal pipes. These were illustrated by small dots extending downward with depth. Moreover, two areas featuring lower color amplitudes, closely situated, were discernible at distances of 4.5 and 103.5 m. This occurrence indicated the presence of two areas affected by leaks.

According to the findings extracted from Figures 16–19, the amplitudes of the hyperbolas within the radar section served as a means to differentiate between metal and PVC pipes within arid zones; however, this method had limited effectiveness in distinguishing these pipe types within leak areas. In contrast, both the enveloped and migrated sections proved to be superior in this regard. These sections demonstrated the ability to discern between these pipes in dry regions and areas affected by leaks—achieving this by exhibiting the highest and weakest signal amplitude reflections within the enveloped sections. Furthermore, the migrated sections demonstrated a contrast of color amplitudes, which accurately signified the positions of these pipes through the use of small dots. As a result, these two techniques hold a distinct advantage over the radar section in terms of their capability to differentiate between these pipe materials in various field conditions.

4. Discussion

Based on the field observations in the study area, it was noted that surface water is present in some regions of the research site, which has led to damage to some buildings. Additionally, the local population has begun displaying indications of various diseases. Therefore, a GPR survey using a 600 MHz antenna was conducted to explore the effectiveness of GPR in detecting the hidden water leak areas along with the associated pipes—which are not easily visible to the naked eye—and to distinguish between the different types of pipe materials within the different leak conditions. We chose the 600 MHz antenna frequency for a high-resolution subsurface image. Reflex software was utilized to process the data, aiming to enhance the signal-to-noise ratio and produce a clear radar section that could be easily interpreted. FDTD numerical modeling was utilized using GprMax software to simulate the hidden metal and PVC pipes within dry and leak areas and produce different simulated images for both scenarios. We compared the radar profiles produced by numerical modeling, serving as a distinctive fingerprint, and those obtained by GPR instruments at particular locations. Furthermore, we applied the migration process on the simulated and field profiles. Additionally, we conducted a comparison between the migrated simulated profiles, which functioned as a visual fingerprint, and the field profiles acquired in the study area to enhance the visibility of the leaky area's characteristics and accurately determine the exact position of the pipes.

The paper discusses methods designed to enhance the differentiation of the underground pipes to ensure proper maintenance and handling. While radar sections can offer effectiveness in some cases, the presence of leaks surrounding the pipes can make their

identification more challenging. Therefore, this study examined different techniques, including trace analysis, hyperbolic reflection analysis, and envelope and migration analysis, which played a significantly more substantial role in this study as they introduced a new application for detecting pipes within leak areas.

The limitation of this study is that only two pipe materials, metal and PVC pipes, were present in the study area, leaving uncertainty regarding whether the GPR method can distinguish between a cluster of pipes made from other materials. To address this limitation and evaluate the effectiveness of the GPR method on different pipe materials, it will be necessary to test the method in another area characterized by various pipe types.

5. Conclusions

This study effectively investigated how the GPR method can be an affordable and non-destructive geophysical technique, using a 600 MHz antenna frequency for identifying water leak areas and various types of underground pipes in the El Hammam region on Egypt's northwest coast. Additionally, it introduced a new application of envelope and migration techniques to precisely distinguish between metal and PVC pipes used to transmit fresh and sewage water, especially within the leak areas in the designated study area. According to the radar sections produced from the GPR survey, it can be concluded that the leak areas were primarily concentrated in the study area's northeast and southeast regions, with some dispersed throughout other parts. Additionally, it revealed that distinguishing between metal and PVC pipes within the dry zones of the study area was straightforward, but this became more challenging in the leaky areas. Furthermore, it can be inferred that metal pipes produce a significant amplitude reflection, regardless of whether they are leaking or not, compared to PVC pipes. The presence of metal pipes causes a substantial change in the dielectric constant, leading to a strong reflection of radar signals and the creation of large hyperbolas in the GPR cross-section. In contrast, PVC pipes are typically transparent; nevertheless, the air or water inside the pipe can reflect radar signals, resulting in relatively weak hyperbolas compared to those produced by metal pipes in the GPR cross-section.

The analysis of the radar profiles generated through numerical modeling and obtained from the GPR scans conducted in a specific area revealed that a water pipe leak caused interference in the wave reflection due to the saturation of the soil. This deviation is distinct from the characteristic hyperbolic pattern exhibited by an intact pipe in both types of radar profiles. The compelling results obtained from simulations and practical experiments and a sufficient technical understanding can enhance operational efficiency in identifying and locating hidden leaky pipes. The simulated models were compared to image-matching fingerprints, revealing a strong correlation between the simulated and acquired radar profiles. As a result, this facilitated the identification, mapping, and differentiation of the concealed leak areas and the various pipe materials under field conditions. After employing migration on the simulated and field data, it was possible to enhance the visibility of the leaky area's characteristics and accurately determine the exact position of the pipes. Surprisingly, the outcomes from the fieldwork in the real-world setting aligned well with the results obtained through numerical modeling simulations conducted under ideal conditions.

We applied various techniques to address the challenge of discerning between metal and PVC pipes. Results showed that all of the techniques employed effectively differentiated between metal and PVC pipes in dry regions. Notably, the trace and envelope analysis techniques proved most adept at distinguishing between these pipe types in leaky areas through their amplitude reflections. Additionally, the migration technique enhanced the visibility of reflection within leaky regions and accurately determined the precise pipe positions. This method also successfully differentiated between distinct pipes based on their color amplitude. In conclusion, based on previous validations, GPR is a valuable close-range sensing tool for efficiently detecting water pipe leaks and iden-

tifying the different types of pipe materials through these leak areas, surpassing other non-destructive technologies.

Author Contributions: Conceptualization, M.G., Q.D., J.Z. and C.F.; methodology, M.G. and A.A.E.-R.; software, M.G., S.E. and A.A.E.-R.; investigation, M.G., Q.D. and J.Z.; writing—original draft preparation, M.G.; writing—review and editing, M.G., Q.D., J.Z., C.F., S.E. and A.A.E.-R.; visualization, M.G.; supervision, Q.D. All authors have read and agreed to the published version of the manuscript.

Funding: This research was financially supported by the National Key R&D Program of China (Grant No. 2022YFF0706200). M.G. was also supported by the CAS-TWAS president doctoral fellowship program for this research.

Data Availability Statement: Data related to this study are accessible and can be acquired by contacting the corresponding author.

Acknowledgments: We extend our appreciation to Ahmed Gaber, Port-Said University, Egypt, for his valuable assistance in acquiring the GPR field data. We are also very appreciative of the Chief Editor for managing the manuscript. Additionally, we would like to extend our thanks to the associate editors and anonymous reviewers for their constructive comments and valuable suggestions, which significantly contributed to enhancing the final version of the manuscript.

Conflicts of Interest: The researchers declare no conflict of interest.

References

1. Karoui, T.; Jeong, S.-Y.; Jeong, Y.-H.; Kim, D.-S. Experimental study of ground subsidence mechanism caused by sewer pipe cracks. *Appl. Sci.* **2018**, *8*, 679. [CrossRef]
2. Brennan, M.J.; Joseph, P.F.; Muggleton, J.M.; Gao, Y. *Some Recent Research Results on the Use of Acoustic Methods to Detect Water Leaks in Buried Plastic Water Pipes*; Institute of Sound Vibration Research, University of Southampton: Southampton, UK, 2008; pp. 1–7.
3. Juliano, T.M.; Meegoda, J.N.; Watts, D.J. Acoustic emission leak detection on a metal pipeline buried in sandy soil. *J. Pipeline Syst. Eng.* **2013**, *4*, 149–155. [CrossRef]
4. Atef, A.; Zayed, T.; Hawari, A.; Khader, M.; Moselhi, O. Multi-tier method using infrared photography and GPR to detect and locate water leaks. *Autom. Constr.* **2016**, *61*, 162–170. [CrossRef]
5. Lee, B.; Oh, S. Modified electrical survey for effective leakage detection at concrete hydraulic facilities. *J. Appl. Geophys.* **2018**, *149*, 114–130. [CrossRef]
6. Dong, L.; Carnalla, S.; Shinozuka, M. GPR survey for pipe leakage detection: Experimental and analytical study. In Proceedings of the Nondestructive Characterization for Composite Materials, Aerospace Engineering, Civil Infrastructure, and Homeland Security, San Diego, CA, USA, 4 April 2012; pp. 96–102.
7. Hong, W.-T.; Kang, S.; Lee, S.J.; Lee, J.-S. Analyses of GPR signals for characterization of ground conditions in urban areas. *J. Appl. Geophys.* **2018**, *152*, 65–76. [CrossRef]
8. Crocco, L.; Soldovieri, F.; Millington, T.; Cassidy, N.J. Bistatic tomographic GPR imaging for incipient pipeline leakage evaluation. *Prog. Electromagn. Res.* **2010**, *101*, 307–321. [CrossRef]
9. Daniels, D.J. *Ground Penetrating Radar*, 2nd ed.; Institution of Electrical Engineers: London, UK, 2004; Volume 1.
10. Amran, T.; Amin, M.; Ahmad, M.; Sani, S.; Masenwat, N.; Bundak, C.; Singoi, C. A study on detection water leakage of underground metal and PVC pipes using ground penetrating radar. In Proceedings of the IOP Conference Series: Materials Science and Engineering; Universiti Teknologi Malaysia: Skudai, Johor, Malaysia, 2019; p. 012012.
11. Hunaidi, O.; Giamou, P. Ground-penetrating radar for detection of leaks in buried plastic water distribution pipes. In Proceedings of the Seventh International Conference on Ground Penetrating Radar, Lawrence, KS, USA, 27–30 May 1998; pp. 783–786.
12. Shaikh, S.A.; Tian, G.; Shi, Z.; Zhao, W.; Junejo, S. Frequency band adjustment match filtering based on variable frequency GPR antennas pairing scheme for shallow subsurface investigations. *J. Appl. Geophys.* **2018**, *149*, 42–51. [CrossRef]
13. Ayala-Cabrera, D.; Herrera, M.; Izquierdo, J.; Perez-Garcia, R. Location of buried plastic pipes using multi-agent support based on GPR images. *J. Appl. Geophys.* **2011**, *75*, 679–686. [CrossRef]
14. Santos, V.R.N.; Teixeira, F.L. Application of time-reversal-based processing techniques to enhance detection of GPR targets. *J. Appl. Geophys.* **2017**, *146*, 80–94. [CrossRef]
15. Annan, A.; Cosway, S.; Redman, J. Water table detection with ground-penetrating radar. In *SEG Technical Program Expanded Abstracts*; Society of Exploration Geophysicists: Houston, TX, USA, 1991; pp. 494–496.
16. Abd El-Gawad, A.; Helaly, A.; Abd El-Latif, M. Application of geoelectrical measurements for detecting the ground-water seepage in clay quarry at Helwan, southeastern Cairo, Egypt. *NRIAG J. Astron.* **2018**, *7*, 377–389. [CrossRef]
17. Araffa, S.A.; Mohamadin, M.I.; Saleh Sabet, H.; Takey, M.S. Geophysical interpretation for groundwater exploration around Hurghada area, Egypt. *NRIAG J. Astron.* **2019**, *8*, 171–179. [CrossRef]
18. Alaminiokuma, G.; Chaanda, M. Geophysical Investigation of Structural Failures Using Electrical Resistivity Tomography: A Case Study of Buildings in FUPRE, Nigeria. *J. Earth Sci. Geotech. Eng.* **2020**, *10*, 15–33.

19. Gemail, K.; Shebl, S.; Attwa, M.; Soliman, S.A.; Azab, A.; Farag, M. Geotechnical assessment of fractured limestone bedrock using DC resistivity method: A case study at New Minia City, Egypt. *NRIAG J. Astron. Geophys.* **2020**, *9*, 272–279. [CrossRef]
20. Panisova, J.; Murín, I.; Pašteka, R.; Haličková, J.; Brunčák, P.; Pohánka, V.; Papčo, J.; Milo, P. Geophysical fingerprints of shallow cultural structures from microgravity and GPR measurements in the Church of St. George, Svätý Jur, Slovakia. *J. Appl. Geophys.* **2016**, *127*, 102–111. [CrossRef]
21. Qin, T.; Zhao, Y.; Lin, G.; Hu, S.; An, C.; Geng, D.; Rao, C. Underwater archaeological investigation using ground penetrating radar: A case analysis of Shanglinhu Yue Kiln sites (China). *J. Appl. Geophys.* **2018**, *154*, 11–19. [CrossRef]
22. Zhang, J.; Yang, W.; Hu, S.; Lin, Y.; Fang, G.; Li, C.; Peng, W.; Zhu, S.; He, Z.; Zhou, B. Volcanic history of the Imbrium basin: A close-up view from the lunar rover Yutu. *Proc. Natl. Acad. Sci. USA* **2015**, *112*, 5342–5347. [CrossRef] [PubMed]
23. Zhang, J.; Zhou, B.; Lin, Y.; Zhu, M.-H.; Song, H.; Dong, Z.; Gao, Y.; Di, K.; Yang, W.; Lin, H. Lunar regolith and substructure at Chang'E-4 landing site in South Pole–Aitken basin. *Nat. Astron.* **2021**, *5*, 25–30. [CrossRef]
24. Li, C.; Zheng, Y.; Wang, X.; Zhang, J.; Wang, Y.; Chen, L.; Zhang, L.; Zhao, P.; Liu, Y.; Lv, W. Layered subsurface in Utopia Basin of Mars revealed by Zhurong rover radar. *Nature* **2022**, *610*, 308–312. [CrossRef]
25. Anbazhagan, P.; Dixit, P.N.; Bharatha, T. Identification of type and degree of railway ballast fouling using ground coupled GPR antennas. *J. Appl. Geophys.* **2016**, *126*, 183–190. [CrossRef]
26. Curioni, G.; Chapman, D.N.; Metje, N. Seasonal variations measured by TDR and GPR on an anthropogenic sandy soil and the implications for utility detection. *J. Appl. Geophys.* **2017**, *141*, 34–46. [CrossRef]
27. Abd El-Gawad, A. Water seepage source at the extension of Tourah clay quarry, southeastern Cairo based on geological and geoelectrical resistivity measurements. *Earth Sci.* **2020**, *9*, 108–116. [CrossRef]
28. De Coster, A.; Medina, J.P.; Nottebaere, M.; Alkhalifeh, K.; Neyt, X.; Vanderdonckt, J.; Lambot, S. Towards an improvement of GPR-based detection of pipes and leaks in water distribution networks. *J. Appl. Geophys.* **2019**, *162*, 138–151. [CrossRef]
29. Prudhomme, K.D.; Khalil, M.A.; Shaw, G.D.; Speece, M.A.; Zodrow, K.R.; Malloy, T.M. Integrated geophysical methods to characterize urban subsidence in Butte, Montana, USA. *J. Appl. Geophys.* **2019**, *164*, 87–105. [CrossRef]
30. Zhang, J.-X.; Zhang, N.; Xu, Y.-S. Data on point cloud scanning and ground radar of composite lining in jointly constructed tunnel. *Data Brief* **2022**, *41*, 107993. [CrossRef] [PubMed]
31. Powers, M.H.; Olhoeft, G.R. Modeling the GPR response of leaking buried pipes. In Proceedings of the 9th EEGS Symposium on the Application of Geophysics to Engineering and Environmental Problems, Keystone, CO, USA, 28 April 1996. cp-205-00057.
32. Eiswirth, M.; Heske, C.; Burn, S.; De Silva, D. New methods for water pipeline assessment. In Proceedings of the IWA 2nd World Water Congress, Berlin, Germany, 15–19 October 2001; p. 8.
33. Stampolidis, A.; Soupios, P.; Vallianatos, F.; Tsokas, G. Detection of leaks in buried plastic water distribution pipes in urban places-a case study. In Proceedings of the 2nd International Workshop on Advanced Ground Penetrating Radar, Delft, The Netherlands, 14–16 May 2003; pp. 120–124.
34. Simi, A.; Bracciali, S.; Manacorda, G. Hough transform based automatic pipe detection for array GPR: Algorithm development and on-site tests. In Proceedings of the IEEE Radar Conference, Rome, Italy, 26–30 May 2008; pp. 1–6.
35. Tavera, M. Aplicación del Georadar para la Mejora del Rendimiento de una Red Hídrica. Master's Thesis, Universitat Politècnica de València, València, España, 2008.
36. Lai, W.W.; Chang, R.K.; Sham, J.F.; Pang, K. Perturbation mapping of water leak in buried water pipes via laboratory validation experiments with high-frequency ground penetrating radar (GPR). *Tunn. Undergr. Space Technol.* **2016**, *52*, 157–167. [CrossRef]
37. Liu, Y.; Shi, Z. Mapping water pipeline leakage by ground-penetrating radar diffraction imaging. *Geophysics* **2022**, *87*, WB1–WB7. [CrossRef]
38. Lam, C.; Zhou, W. Statistical analyses of incidents on onshore gas transmission pipelines based on PHMSA database. *Int. J. Press. Vessel. Pip.* **2016**, *145*, 29–40. [CrossRef]
39. Lee, K.-F.; Wang, T.-K.; Kang, Y.-M.; Wang, C.-S.; Lin, K.-A. Identification of pipelines from the secondary reflect wave travel time of ground-penetrating radar waves. *J. Mar. Sci. Technol.* **2013**, *21*, 6.
40. dos Santos, V.R.N.; Al-Nuaimy, W.; Porsani, J.L.; Hirata, N.S.T.; Alzubi, H.S. Spectral analysis of ground penetrating radar signals in concrete, metallic and plastic targets. *J. Appl. Geophys.* **2014**, *100*, 32–43. [CrossRef]
41. Kamal, N.H.B.M.; Amin, Z.M.; Mohamad, N.B. The effect of ground penetrating radar (GPR) image reflection on different pipes and soil. In Proceedings of the IOP Conference Series: Earth and Environmental Science, Kuala Lumpur, Malaysia, 20–21 October 2020; p. 012093.
42. Said, R. *The Geology of Egypt*, 1st ed.; Editor Said, A., Ed.; Balkema: Rotterdam, The Netherlands, 1990; p. 734.
43. Shata, A.A.; El Shazly, M.M.; Attia, S.H.; Abouel Fetouh, M. The geology of Quaternary deposits and their mutual relation to soil formations in the fringes west of the Nile Delta, Egypt. *Desert Inst. Bull.* **1978**, *28*, 43–77.
44. Raslan, S.M. Geomorphological and Hydrogeological Studies on Some Localities along the Northwestern Coast of Egypt. Master's Thesis, Faculty of Science, Menoufia University, Menofia, Egypt, 1995.
45. Hammad, F.A. The Geology of the Soil and Water Resources in the Area between Ras El-Hekma and Ras Alam El-Rum (Western Mediterranean Littoral Zone, Egypt). Ph.D. Thesis, Faculty of Science, Cairo University, Cairo, Egypt, 1972.
46. Selim, A.A. Origin and lithification of the Pleistocene carbonates of the Salum area, western coastal plain of Egypt. *J. Sediment. Res.* **1974**, *44*, 70–78.

47. Ezzeldin, H.A.; Kamal, A.; Reda, A.M.; Guindy, K.; El-Shamy, I. Assessment of factors affecting the groundwater quality in El-Hammam Area, northwest coast of Egypt. *Middle East J. Appl. Sci.* **2019**, *8*, 798–819.
48. Akinsunmade, A.; Karczewski, J.; Mazurkiewicz, E.; Tomecka-Suchoń, S. Finite-difference time domain (FDTD) modeling of ground penetrating radar pulse energy for locating burial sites. *Acta Geophys.* **2019**, *67*, 1945–1953. [CrossRef]
49. Holden, J.; Burt, T.P.; Vilas, M. Application of ground penetrating radar to the identification of subsurface piping in blanket peat. *Earth Surf. Process. Landf.* **2002**, *27*, 235–249. [CrossRef]
50. Jol, H.M.; Smith, D.G. Ground penetrating radar of northern lacustrine deltas. *Can. J. Earth Sci.* **1991**, *28*, 1939–1947. [CrossRef]
51. Di Prinzio, M.; Bittelli, M.; Castellarin, A.; Pisa, P.R. Application of GPR to the monitoring of river embankments. *J. Appl. Geophys.* **2010**, *71*, 53–61. [CrossRef]
52. Jol, H.M. *Ground Penetrating Radar Theory and Applications*; Elsevier: Amsterdam, The Netherlands, 2008.
53. Utsi, E.C. *Ground Penetrating Radar: Theory and Practice*; Butterworth-Heinemann: Oxford, UK, 2017.
54. Eyuboglu, S.; Mahdi, H.; Al-Shukri, H. Detection of water leaks using ground penetrating radar. In Proceedings of the Third International Conference on Applied Geophysics, Orlando, FL, USA, 8–12 December 2003; pp. 8–12.
55. Kuo, S.-S.; Zhao, L.; Mahgoub, H.S.; Suarez, P.F. *Investigation of Ground Penetrating Radar for Detection of Leaking Pipelines under Roadway Pavements and Development of Fiber-Wrapping Repair Technique*; University of Central Florida: Orlando, FL, USA, 2005.
56. Fariza, N.A.Y. Retrieval of Soil Physical Parameter from Multi Band GPR Dataset. Undergraduate Thesis, Universiti Teknologi Malaysia, Skudai, Malaysia, 2016.
57. Neal, A. Ground-penetrating radar and its use in sedimentology: Principles, problems and progress. *Earth-Sci. Rev.* **2004**, *66*, 261–330. [CrossRef]
58. Ferrara, C.; Barone, P.M.; Salvati, L.; Pettinelli, E. Ground penetrating radar as remote sensing technique to investigate the root system architecture. *Appl. Ecol. Environ. Res.* **2014**, *12*, 695–702. [CrossRef]
59. Sandmeier, K. *REFLEXW: Windows TM 9x/NT/2000/XP/7/8-Program for the Processing of Seismic, Acoustic or Electromagnetic Reflection, Refraction and Transmission Data*; Sandmeier Scientific Software: Karlsruhe, Germany, 2014.
60. Olhoeft, G.R. Maximizing the information return from ground penetrating radar. *J. Appl. Geophys.* **2000**, *43*, 175–187. [CrossRef]
61. Annan, A.P. Ground-penetrating radar. In *Near-Surface Geophysics*; Investigations in Geophysics; Society of Exploration Geophysicists: Tulsa, OK, USA, 2005; Volume 13, pp. 357–438.
62. Cassidy, N.J. Ground penetrating radar data processing, modeling and analysis. In *Ground Penetrating Radar: Theory and Applications*; Jol, H.M., Ed.; Elsevier: Amsterdam, Netherlands, 2009; pp. 141–176.
63. Bristow, C.S. Ground penetrating radar. In *Treatise on Geomorphology*; Shroder, J.F., Ed.; Academic Press: San Diego, CA, USA, 2013; Volume 14, pp. 183–194.
64. Davis, J.L.; Annan, A.P. Ground-penetrating radar for high-resolution mapping of soil and rock stratigraphy 1. *Geophys. Prospect.* **1989**, *37*, 531–551. [CrossRef]
65. Nye, J.F.; Berry, M.V. Dislocations in wave trains. *Proc. R. Soc. London. A. Math. Phys. Sci.* **1974**, *336*, 165–190.
66. Stolt, R.H. Migration by Fourier transform. *Geophysics* **1978**, *43*, 23–48. [CrossRef]
67. Smitha, N.; Ullas Bharadwaj, D.R.; Abilash, S.; Sridhara, S.N.; Singh, V. Kirchhoff and FK migration to focus ground penetrating radar images. *Int. J. Geo-Eng.* **2016**, *7*, 1–12. [CrossRef]
68. GSSI, G.S.S., Inc. *Utility Locating Handbook*; MN72-615 Rev B; GSSI: Nashua, United States, 2018.
69. Liu, Y.; Greenwood, A.; Hetényi, G.; Baron, L.; Holliger, K. High-resolution seismic reflection survey crossing the insubric line into the Ivrea-Verbano Zone: Novel approaches for interpreting the seismic response of steeply dipping structures. *Tectonophysics* **2021**, *816*, 229035. [CrossRef]